RSC Advances

ROYAL SOCIETY OF CHEMISTRY

www.rsc.org/advances

A table of contents entry

α-MnO_2-$LaNiO_3$/CNTs as one integrated hybrid exhibits enhanced reactivity towards ORR and OER. Electrons are directly transferred by CNTs conductor.

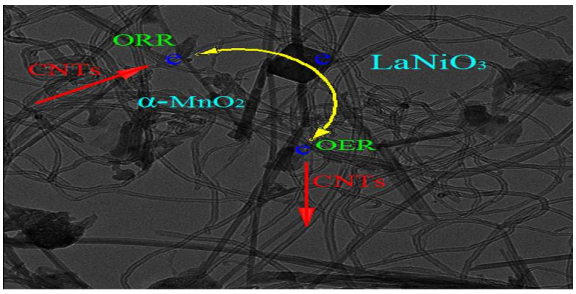

A table of contents entry

α-MnO_2-$LaNiO_3$/CNTs as one integrated hybrid exhibits enhanced reactivity towards ORR and OER. Electrons are directly transferred by CNTs conductor.

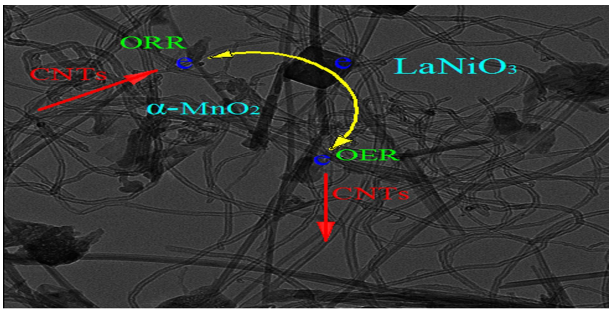

A bifunctional electrocatalyst α-MnO_2-$LaNiO_3$/carbon nanotubes composite for rechargeable zinc-air batteries

Hongyun Ma, Baoguo Wang*

Department of Chemical Engineering, Tsinghua University, Beijing 100084, China

Abstract: Development of highly active, non-precious, electrochemical catalysts is needed to optimize rechargeable zinc-air battery electrodes. Herein, we fabricate bifunctional electrocatalysts α-MnO_2-$LaNiO_3$/carbon nanotubes (CNTs) composite towards the activity of the oxygen reduction reaction (ORR) and oxygen evolution reaction (OER). CNTs are used to support the bifunctional catalysts as one integrated material. The chemical and physical characterizations of the bifunctional catalyst are characterized by X-ray diffraction (XRD), X-ray photoelectron spectroscopy (XPS), transmission electron microscope (TEM), and scanning electron microscopy (SEM). The electrochemical properties of the bifunctional catalyst tested by a rotating disc electrode system revealed enhanced catalytic activity toward both the ORR and OER. Four-electron reduction pathway contributes to the ORR process at different rotation speeds indicating an effective catalytic activity. A rechargeable zinc-air battery using the bifunctional catalyst achieved a maximum power density of 55.1 mW cm^{-2}, and its voltage polarization showed a 1.4% decrease in discharge and a 4.8% increase in charge after 75 charge-discharge (C-D) cycles. The charge transfer resistance for the ORR and OER catalyzed by the bifunctional catalyst increased from 1.24 to 4.68 Ω after 75 C-D cycles. The bifunctional electrocatalysts show satisfactory performance

* Corresponding author. Tel./fax: +86 10 62788777.
Email addresses: bgwang@mail.tsinghua.edu.cn

in an electrically rechargeable zinc-air battery.

Keywords: α-MnO_2-$LaNiO_3$/CNTs; Bifunctional electrocatalyst; Oxygen reduction reaction; Oxygen evolution reaction; Electrically rechargeable zinc-air battery

1. Introduction

Rechargeable metal-air batteries including Li-air batteries[1-3] and zinc-air batteries[4-6] are regarded as potential alternatives for both mobile and stationary future energy-storage applications.[7] The theoretical specific capacity and energy of Li-air batteries are 3862 mAh g^{-1} and 5200 Wh kg^{-1}_{-Li}, respectively.[1-3,8,9] Electrically rechargeable zinc-air batteries are also considered promising energy-storage systems because of their extremely high energy density (> 400 W h kg^{-1}), safety, low cost, environmental friendliness, and light weight.[4-6,10,11] In electrically rechargeable metal-air battery systems, the critical oxygen reduction reaction (ORR) and oxygen evolution reaction (OER) occur at the air cathode during battery discharge and charge processes, respectively. However, the sluggish kinetics and large overpotential of the ORR/OER limit the rate performance of metal-air batteries, which has seriously limited their development and commercialization.[12] To improve the kinetic properties of the ORR/OER, bifunctional catalysts with high activity, long lifetime and good efficiency have attracted much attention worldwide.

Currently, noble metal catalysts such as Pt, Pt-Pd, and Au have high reactivity for the ORR and catalysts such as IrO_2 provide good OER activity.[10,13,14] However, the

high cost of these catalysts limits their practical application. Non-precious catalysts such as transition metal oxides, carbon-based materials, and perovskite oxides have been investigated widely as less expensive alternatives to noble metal catalysts.[4,7,13] Among transition metal oxides, manganese oxides (MnO_x) and cobalt oxides (CoO_x) have been the most extensively researched because of their low cost and high efficiency.[4] To date, MnO_2 is the most active electrocatalyst for the ORR among all MnO_x, with the activity of different types of MnO_x following the order α- > β- > γ-MnO_2 in alkaline solution.[4,15] Perovskites with the chemical formula ABO_3 such as $LaNiO_3$ and $LaCoO_3$ show high reactivity for the OER and are inexpensive.[7,13] So far, most studies have focused only on the catalysts and the charge transfer and electronic conduction processes are usually studied separately, therefore it is difficult to decrease the electronic hopping resistance during ORR/OER processes.

In this paper, we propose a practical approach to prepare bifunctional catalysts for both the ORR and OER by integrating ORR and OER electrocatalysts with carbon nanotubes (CNTs) as an electronic conductor, and then fabricate an air electrode for electrically rechargeable metal-air batteries. The electrocatalyst provides active sites for both ORR and OER processes, and simultaneously, the electrons required by the ORR or produced from the OER are directly transferred to the CNTs current collector. As a result, the electronic hopping resistance in this integrated material is obviously reduced. To increase the number of active sites and adsorb more reactant on the catalyst surface, nanoparticles of α-MnO_2 and $LaNiO_3$ were adsorbed on CNTs. Using CNTs as an electronic conductor modifies the poor electrical conductivity of α-MnO_2

nanorods and $LaNiO_3$ nanoparticles to decrease the electronic hopping resistance. The bifunctional catalyst α-MnO_2-$LaNiO_3$/CNTs was prepared and characterized. The activity of the bifunctional catalyst for the ORR and OER in alkaline solution is tested using a rotating disc electrode (RDE) system. The electrochemical performance of the bifunctional catalyst in a custom-made zinc-air battery is evaluated.

2. Experimental

2.1. Synthesis of bifunctional catalyst α-MnO_2-$LaNiO_3$/CNTs

Perovskite oxide $LaNiO_3$ nanoparticles were prepared by a modified sol-gel method.[16] Equimolar amounts of $La(NO_3)_3 \cdot 6H_2O$ (0.005 mol, Yongda Chemical Co., Ltd, Tianjin. China) and $Ni(NO_3)_2 \cdot 6H_2O$ (0.005 mol, Beijing Modern Eastern Fine Chemical Co., Ltd) were dissolved in a small amount of deionized water. Polydentate ligand citric acid (0.01 mol, Beijing Modern Oriental Fine Chemistry Co., Ltd) was dissolved in the above solution. The solution was heated at 90 °C for 6 h to give the powder precursor upon drying. The powder was calcined at 900 °C for 5 h under an air atmosphere. The temperature was increased at a rate of 10 °C min^{-1}.

α-MnO_2 nanorods were synthesized by hydrothermal treatment.[17,18] $MnSO_4 \cdot H_2O$ (1.352 g, Beijing Chemical Works), $(NH_4)_2S_2O_8$ (1.824 g, Beijing Modern Oriental Fine Chemistry Co., Ltd), and $(NH_4)_2SO_4$ (1.98 g, Beijing Modern Oriental Fine Chemistry Co., Ltd) were added to deionized water (40 mL) at room temperature and ultrasonically dispersed for 30 min. When a homogeneous solution was obtained, the mixture was transferred into a 100-mL Teflon-lined autoclave, and then kept at 120 °C for 12 h. The resulting black product was filtered, purified with deionized water, and

dried at 80 °C in air for 24 h.

A dispersion of CNTs (1g; 210 m^2 g^{-1}, CNano Technology Ltd, Beijing, China) was added to a mixture of α-MnO_2 nanorods (0.2 g) and $LaNiO_3$ (0.2 g) nanoparticles in ethanol and deionized water (volume ratio 1:1). The mixture was ultrasonically stirred at 60 °C for 30 min. Ethanol and water were then removed by increasing the temperature at a rate of 5 °C min^{-1} to the desired temperature of 80 °C for 2 h. The resulting powder was ground with an agate mortar. Samples with different molar or weight ratios of bifunctional catalysts and CNTs were prepared with the same procedures as above.

2.2. Catalyst characterization

$LaNiO_3$, α-MnO_2, and the bifunctional catalyst were characterized by X-ray diffraction (XRD, Bruker D8 Advance, Bruker, Germany), infrared spectroscopy (FTIR, Bruker Tensor 27, Bruker, Germany) using KBr pellets, and scanning electron microscopy (SEM, JEOL, JSM-7401F, Japan). The diffraction angle (2θ) range for XRD between 10° and 75° was scanned continuously. The scanning range for FTIR spectra was from 400 to 4000 cm^{-1}. Transmission Electron Microscopy (TEM) characterizations were performed using a HITACH 7700 TEM instrument (Japan). High-resolution X-ray photoelectron spectroscopy (XPS) data were obtained using a Quantera SXM instrument (Al Kα radiation, $h\nu = 1484.6\,\text{eV}$). The specific surface areas of the samples were obtained by BET method (NOVA 2200e, Quantachrome Instruments, USA). The samples were degassed for 12 h at 150 °C and then adsorbed with nitrogen gas at -200 °C.

The electrochemical properties of the bifunctional catalyst were measured using reported fuel cell catalyst testing methods.[19,20] First, catalyst ink was prepared by dispersing catalyst (40 mg) in EtOH (10 mL) containing 60% polytetrafluoroethylene (PTFE) solution (25 μL) so there was ~24 wt% PTFE to that of the catalyst. Next, catalyst ink (25 μL) was uniformly loaded onto a glass carbon electrode with a diameter of 5 mm to give coverage of ~0.5 mg cm^{-2}. The ink was dried slowly by trial and error with a small hot air fan until the catalyst distributed uniformly across the electrode surface. The resulting electrode was electrochemically evaluated by linear sweep voltammetry (LSV) at different rotation speeds, and repeated cyclic voltammograms in a three-electrode electrochemical cell. The reference, counter and working electrodes were an Hg/HgO electrode filled with 1 M KOH, large Pt plate and glassy carbon electrode, respectively. LSV was carried out at a scan rate of 10 mV s^{-1} in O_2-saturated 1.0 M KOH solution. The solution was bubbled with O_2 for more than 30 min before taking measurements. Repeated cyclic voltammograms were obtained from −0.6 to 0.8 V *vs*. Hg/HgO at a scan rate of 10 mV s^{-1}.

The electrochemical rechargeable zinc-air battery was tested in a custom-made electrochemical cell. Polarization and power density curves of the zinc-air battery system, charge-discharge cycles, and electrochemical impedance spectroscopy (EIS) curves were obtained from the device. Polarization curves and power density data were collected at different current densities. EIS was measured over the frequency range of 0.1–10^5 Hz with a disturbance voltage of 10 mV. Besides, in order to gain more information of the charge transfer resistances in the anode and cathode reactions,

galvnostatical EIS was performed at different load current densities from 100 mHz to 100 kHz with a disturbing current of 0.5 mA.

2.3. Preparation of the air electrode

Catalyst inks were prepared by mixing the α-MnO_2-$LaNiO_3$/CNTs catalyst with a weight ratio of 3:1:6 in a mixture of deionized water and ethanol (volume ratio 1:1). A PTFE emulsion (60%, Hesen Co., Ltd., Shanghai, China) was used as a wet-proofing agent and binder (the weight ratio 25%). PTFE emulsion was sprayed onto the carbon paper and then pressed onto one side of the Ni mesh substrate (60 order, Ruilida Ni Co., Ltd.) to form a gas diffusion layer (GDL). The catalyst inks were sprayed onto the other side of the Ni mesh to form a catalytic layer. The air electrode (the thickness: 1.2 mm) was finally pressed for 30 min under a pressure of 20 MPa and then dried at 80 °C for 2 h.

2.4. Fabrication of the zinc-air battery

A polished zinc plate (7 cm^2, Institute of Metal Research, Beijing, China) and some of the custom-made air electrode were used as the negative and positive electrode, respectively. The schematic diagram of the zinc-air battery system is shown in Fig. 1. The area of the GDL exposed to the air was about 7 cm^2 and the same area of the catalytic layer was exposed to the electrolyte. The electrolyte used in the zinc-air battery system was 0.4 M ZnO dissolved in 6 M KOH. As reported before,[10,14] a charge-discharge experiment was carried out by discharging or charging for 300 s in each state of the zinc-air battery system at a current density of 20 mA cm^{-2}.

3. Results and discussion

3.1. Characterization of the bifunctional catalyst

The physical and chemical characteristics of the electrochemical catalysts were examined by FTIR spectroscopy, XRD, SEM, TEM, and XPS. Fig. 2(a) and (b) show XRD patterns of α-MnO_2 and $LaNiO_3$ (15.73 m^2/g), respectively. At 900 °C, the XRD pattern of $LaNiO_3$ is consistent with a single phase. No peaks attributed to $LaNi_2O_4$, La_2O_3, or Ni-O are observed.[21] The peaks observed in the pattern of α-MnO_2 can all be indexed to the pure tetragonal phase α-MnO_2.[17,18,22] The FTIR spectrum obtained for $LaNiO_3$ calcined at 900 °C is shown in Fig. 2(c). There is no organic impurity evident in the region of 400–4000 cm^{-1}, which confirms the high purity of the $LaNiO_3$ powder. All of the major peaks observed are attributed to the peroviskite oxide $LaNiO_3$ and the stretching vibration of the Ni-O interaction appears at 601 cm^{-1}.[21,23] Fig. 2(d) shows the XPS spectra of the C, O, La, Ni, and Mn peak regions in catalyst hybrid. No evident peaks are observed associating with contamination, which was good agreement with XRD analysis. In Fig. 2(e), C 1s peak at 284.56 eV is mainly due to the CNTs used as the electronic conductor.[24] O 1s profile (see Fig. 2(f)) in the catalyst hybrid is obvious at 531.15 eV. In Fig. 2(g), it is much more complex to analyze La and Ni peaks for the overlapping of Ni $2p_{3/2}$ and La $3d_{3/2}$ peaks.[16] In the oxygen environment, the most intense of Ni $2p_{3/2}$ associating with the characteristics of Ni^{2+}/Ni^{3+} ions appeared at 855.1 eV.[16] The two typical peaks of La $3d_{5/2}$ locate at 833.8 and 837.4 eV, although the peak at lower binding energy was not obvious.[25] Mn $2p_{3/2}$ and Mn $2p_{1/2}$ (Fig. 2(h)) in MnO_2 exhibited two major peaks with binding energy

values at 642.2 and 654.0 eV, respectively.[11] Besides, it is important to mention that no changes were observed for each material before and after the preparation of bifunctional catalyst. The XPS results suggest CNTs and bifunctional catalysts do not react chemically with each other during ultrasonic preparation steps and the interaction between them was most likely associating with the physical adsorption.

Typical crystals of α-MnO_2 (5.85 m^2 g^{-1}) are presented in Fig. 3(a), and are mainly nanorods. Meanwhile, an SEM image of $LaNiO_3$ (Fig. 3(b)) shows uniform nanoparticles with an average size of ~120 nm, which can be also confirmed in TEM image in Fig. 3(e). The diameter of CNTs used in the catalyst hybrid is about 25 nm (Fig. 3(c) and (d)). Fig. 3(e) and Fig. 3(f) show the TEM images of $LaNiO_3$/CNTs and α-MnO_2/CNTs, respectively. α-MnO_2 nanorods are well integrated with CNTs. The diameter and length of α-MnO_2 nanorods are ~50 nm and ~250 nm, respectively. $LaNiO_3$ nanoparticles are adsorbed on the surface of CNTs. An SEM and TEM images of the bifunctional catalysts are depicted in Fig. 3(c) and Fig. 3(g), which clearly indicate that $LaNiO_3$ nanoparticles and α-MnO_2 nanorods are integrated by the CNTs. The bifunctional catalysts and conductive network formed by CNTs are combined uniformly as one integrated material. More active sites are supplied for ORR and OER. The morphology of α-MnO_2-$LaNiO_3$/CNTs indicates that the charges transferred after the OER and ORR could be continuously connected to the current collector by the CNTs, which decreases the electronic hopping resistance by this integrated hybrid.

3.2. ORR activity

The electrochemical behaviors of the $(\alpha\text{-}MnO_2)_x\text{-}(LaNiO_3)_y$/CNTs (where x and y represent molar ratio) and $[(\alpha\text{-}MnO_2)_2\text{-}(LaNiO_3)_3]_w/(CNTs)_z$ (where w and z represent weight ratio) catalysts towards the ORR were evaluated by LSV using a RDE (1600 rpm) in the half-cell setup, as illustrated in Fig. 4. Here it was reasonable to say that the influence of oxygen transport on the evaluation of the catalytic activities could be negligible using RDE system with 1600 rpm.[26] Among the five samples, the ORR activity of $(\alpha\text{-}MnO_2)_2\text{-}(LaNiO_3)_3$/CNTs was the highest, which was better than the performance of catalyst $\alpha\text{-}MnO_2$/CNTs towards ORR activity. When the content of CNTs was changed, as shown in Fig. 4(b), $[(\alpha\text{-}MnO_2)_2\text{-}(LaNiO_3)_3]_{40\%}/(CNTs)_{60\%}$ showed the highest current density and exhibited excellent ORR activity. We can reasonably assume that a certain content of CNTs (60%) will be sufficient to fulfill the conductivity of electrons, while the remaining content of catalyst (40%) will provide sufficient catalytic active sites for the ORR.

The electrochemical reaction mechanisms of the ORR and the kinetic parameters of the ORR for the $[(\alpha\text{-}MnO_2)_2\text{-}(LaNiO_3)_3]_{40\%}/(CNTs)_{60\%}$ catalyst were studied with a RDE. The polarization curves of $[(\alpha\text{-}MnO_2)_2\text{-}(LaNiO_3)_3]_{40\%}/(CNTs)_{60\%}$ at rotation speeds of 100–1600 rpm are presented in Fig. 5(a). According to the Koutecky-Levich (K-L) law:

$$\frac{1}{I} = \frac{1}{I_k} + \frac{1}{I_d} \tag{1}$$

$$I_d = 0.62nFAD_{O_2}^{2/3}\nu^{-1/6}C_{O_2}\omega^{1/2} = B\omega^2 \tag{2}$$

$$\frac{1}{I} = \frac{1}{I_k} + \frac{1}{B}\omega^{-1/2} \quad (3)$$

where I_k and I_d are the kinetic current and diffusion-limited current, respectively. ω (rad s^{-1}) is the angular rotation speed of the RDE, n is the number of electrons involved in the ORR process, F is the Faraday constant (96485 C mol^{-1}), A is the electrode area, C_{O_2} is the concentration of O_2 in 1 M KOH solution at 25 °C (0.93×10^{-6} mol cm^{-3}), D_{O_2} is the diffusion coefficient of O_2 in 1 M KOH solution (1.76×10^{-5} cm^2/s), and ν is the kinetic viscosity of the solution at 25 °C (0.01 cm^2 s^{-1}).[27]

The K-L plots measured at potentials of −0.4 V and −0.5 V with different rotation speeds are presented in Fig. 5(b). The kinetic parameters of oxygen reduction reaction can be obtained from the Levich slop. The approximately linear regions with the slope of n~4 are observed, which indicate a quasi four-electron reduction pathway. Similar results were reported before for α-MnO_2 catalyst mixed with carbon powders and Mn species assisted the charge transfer involved in ORR.[11,28] Herein, $[(\alpha\text{-}MnO_2)_2\text{-}(LaNiO_3)_3]_{40\%}/(CNTs)_{60\%}$ (the specific surface area 132.51 m^2 g^{-1}) is an effective catalyst for the air electrode.

3.3. OER activity

The electrochemical behavior of the $(\alpha\text{-}MnO_2)_x\text{-}(LaNiO_3)_y$/CNTs (x and y represent molar ratio) and $[(\alpha\text{-}MnO_2)_3\text{-}(LaNiO_3)_2]_w/(CNTs)_z$ (w and z represent weight ratio) catalysts towards the OER was evaluated by LSV using the half-cell setup. Fig. 6 compared the LSV curves of the bifunctional catalyst $(\alpha\text{-}MnO_2)_x\text{-}(LaNiO_3)_y$/CNTs with different molar and weight ratios. The samples

exhibited the onset potential of OER after anodic peaks at ~550 mV. Similar peaks were reported before and they were associated with the spinel electrode,[27] which was likely the adsorption process of OH^- to the surface of spinel catalyst. The OER activity of $(\alpha\text{-}MnO_2)_3\text{-}(LaNiO_3)_2$/CNTs (CNTs 50%) was the highest (Fig. 6(a)), which was a little better than the performance of $LaNiO_3$/CNTs towards OER activity. When the content of CNTs reached 40% (Fig. 6(b)), the catalyst showed excellent OER activity. Based on these data, the conductivity of electrons promoted by CNTs and the catalytic active sites for the OER were in optimal proportions in $[(\alpha\text{-}MnO_2)_3\text{-}(LaNiO_3)_2]_{60\%}/(CNTs)_{40\%}$.

The performance balance of the ORR, OER, and electron hopping properties can be generally obtained by optimizing the proportions of $\alpha\text{-}MnO_2$, $LaNiO_3$, and CNTs in the electrochemical catalyst. Combining the results of both ORR and OER activity, suitable ranges of x:y and w:z values for the catalyst $[(\alpha\text{-}MnO_2)_x\text{-}(LaNiO_3)_y]_w/(CNTs)_z$ were determined, as shown in Fig. 7. The ratios of x:y from 1:1 to 3:2 and w:z from 1:2 to 3:2 showed high reactivity toward both the ORR (Fig. 7(a)) and OER (Fig. 7(b)). When the proportions of CNTs, $\alpha\text{-}MnO_2$, and $LaNiO_3$ are between the above values, the conductivity of electrons and both ORR and OER activities are excellent for the gas diffusion electrode. When the content of CNTs is decreased, the current density is also decreased probably because of non-continuous electronic conduction by the CNTs. In contrast, when the content of either catalyst becomes lower than the optimal range, there will not be enough catalytic active sites for both the ORR and OER.

3.4. Catalyst stability

Repetitive cyclic voltammetry is an effective way to provide information about the electrochemical stability of a catalyst.[29] Fig. 8 shows the first, 30th, and 100th cycles of the bifunctional catalyst. As an OER electrocatalyst, the current density (at 0.8 V *vs*. Hg/HgO) decreases by 2.3% and 5.3% for the 30th and 100th cycle, respectively. The current density of the ORR (at −0.4 V *vs*. Hg/HgO) decreases by 1.6% after 30 cycles and 2.5% after 100 cycles. Overall, the α-MnO_2-$LaNiO_3$/CNTs catalyst exhibits satisfactory stability for both the ORR and OER.

3.5. Zinc-air battery performance

Polarization and power density curves of the custom-made zinc-air battery system employing bifunctional catalysts and CNTs with different weight ratios: $[(\alpha\text{-}MnO_2)_2\text{-}(LaNiO_3)_3]_{40\%}/(CNT)_{60\%}$ (the cell was numbered as cell #1) and $[(\alpha\text{-}MnO_2)_2\text{-}(LaNiO_3)_3]_{20\%}/(CNT)_{80\%}$ (the cell was numbered as cell #2) are displayed in Fig. 9. For the zinc air battery using catalyst $[(\alpha\text{-}MnO_2)_2\text{-}(LaNiO_3)_3]_{40\%}/(CNT)_{60\%,}$ the cell voltages were as high as 1.0 and 2.3 V for discharge and charge processes at a current density of 30 mA cm^{-2}, respectively. The power density increased with the current density increasing to ~81 mA cm^{-2} but decreased when the current density increased from ~81 to 150 mA cm^{-2}. This was ascribed to the more serious polarization losses at the larger current density. The maximum power density of 55.1 mW cm^{-2} was obtained at a current density of 81 mA cm^{-2} at room temperature. By comparison with the cell #2, both the charge and discharge polarization losses decreased and the power density increased in the cell #1. It was likely ascribed to the

decreased active sites for ORR and OER in the air electrode with the weight ratio of bifunctional catalysts decreasing in cell #2. The results were in good agreement with LSV in the previous section.

To evaluate battery performance, the stability of the catalyst was investigated using charge-discharge (C-D) cycles (Fig. 10). The initial and final voltage plateau values of $E_{discharge}$ and E_{charge} for the catalyst are also shown in Table 1. $E_{discharge}$ and E_{charge} showed a 1.4% decrease and 4.8% increase after 75 C-D cycles, respectively. These results for C-D cycle stability are in good agreement with those from cyclic voltammetry. In contrast, a reported carbon-supported platinum (Pt/C) catalyst[14] suffered a 56% decrease in the discharging process and a 4% increase in the charging process in the equivalent experiment. Another catalyst, MnO_2-nitrogen-doped CNTs,[26] suffered a 20% decrease during discharge and 5% increase during charge after only 50 C-D cycles for 300 s in each state. Therefore, the relative stability of our catalyst shows that it has good rechargeable capability and excellent ORR and OER activities.

To investigate the degradation mechanisms of the zinc-air battery before and after C-D cycles, EIS plots at open circuit potential were performed at the initial, 50^{th}, and 75^{th} cycles; the results are presented in Fig. 11(a) and the equivalent circuit model was shown in Fig. 11(c). R_s is associated with the battery resistance, *e.g.*, electrolyte and contact resistance. R_{ct1} and CPE1 represent the reaction resistance and double-layer capacitance on the zinc anode side. R_{ct2} and CPE2 represent the reaction resistance and double-layer capacitance on the air cathode side. The line at 45° in the

low-frequency region revealed the Warburg diffusion resistance (Z_w). From the fitting results, R_{ct1} and R_{ct2} increased from 0.17 and 1.24 Ω to 0.23 and 4.68 Ω before and after 75 C-D cycles, respectively. And at the 50th cycle, the charge transfer resistances of the air cathode and zinc anode reactions are 3.76 and 0.21 Ω, respectively. The gradually increased charge transfer resistance of R_{ct1} was due to the irreversible morphology of the zinc anode after C-D cycles.[30] Charging the battery may increase R_{ct2} value because of the C-D cycle resulted in some detachment of the ORR catalyst from the supporting material of CNTs in the air cathode.[19,31] Besides, G. Toussaint found that MnO_2 catalyst was dissolved or degraded during the charging process at potentials of more than 0.5 V vs. Hg/HgO/KOH (1 M).[31] Moreover, the galvanostatic EIS plots at different discharge current densities (see Fig. 11(b)) were observed with two distinctive loops including high and low frequency semicircles associating with negative and positive reaction impedances and the similar results were report before.[32] Both semicircles decreased with the current density increasing. It was ascribed to the charge transfer impedances of Zn/Zn^{2+} reaction and ORR.[32] The fitting results with the equivalent circuit models shown in Fig. 11 (c) indicated that the decreasing charge transfer resistance of zinc anode reaction and ORR had a dependency of the overpotential according to the Tafel equation. Therefore, the degradation in the performance of the zinc-air battery system was mainly caused by the gradual deactivation of the catalyst in the air electrode and the irreversible morphology of zinc anode after C-D cycles.

4. Conclusions

Bifunctional electrochemical catalyst α-MnO_2-$LaNiO_3$/CNTs was obtained by integrating α-MnO_2 nanorods and $LaNiO_3$ nanoparticles to the surface of CNTs. α-MnO_2-$LaNiO_3$/CNTs showed enhanced performance for the ORR and OER in alkaline solution. The electrochemical properties of an α-MnO_2-$LaNiO_3$/CNTs hybrid tested by a RDE system revealed better activity towards the ORR and OER than α-MnO_2/CNTs and $LaNiO_3$/CNTs, respectively, which demonstrated a synergistic effect. Four-electron reduction pathway was observed for the ORR at different rotation speeds, which demonstrated a promising electrocatalyst for air electrode. Taking into consideration of the conducting properties of electrons and catalytic active sites, the ranges of x:y from 1:1 to 3:2 and w:z from 1:2 to 3:2 ($[(\alpha\text{-}MnO_2)_x\text{-}(LaNiO_3)_y]_w/(CNTs)_z$ (where x and y represent molar ratio and w and z represent weight ratio)) show higher reactivity toward the ORR and OER than catalysts with other compositions. Battery testing indicated the bifunctional catalyst showed excellent charge-discharge cycle performance with its voltage polarization exhibiting a 1.4% decrease in discharge and 4.8% increase in charge after 75 charge-discharge cycles. The fabricated rechargeable zinc-air battery achieved a maximum power density of 55.1 mW cm^{-2} at a current density of 81 mA cm^{-2}. Cyclic voltammetry results showed that the current density (at 0.8 V *vs*. Hg/HgO) of the OER decreased by 2.3% and 5.3% for the 30th and 100th cycle, respectively. The current density of the ORR (at −0.4 V *vs*. Hg/HgO) decreased by 1.6% after 30 cycles and 2.5% after 100 cycles. The composite electrocatalyst α-MnO_2-$LaNiO_3$/CNTs can effectively improve ORR/OER kinetics and shows potential as an air electrode for

electrically rechargeable metal-air batteries.

Acknowledgments

The authors gratefully acknowledge the financial support from the National Natural Science Foundation of China (21276134) and the National 973 Project (2010CB227202).

References

1. A. K. Thapa and T. Ishihara, *Journal of Power Sources*, 2011, **196**, 7016-7020.
2. C. M. Hayner, X. Zhao and H. H. Kung, *Annual Review of Chemical and Biomolecular Engineering*, 2012, **3**, 445-471.
3. T. Ogasawara, A. Débart, M. Holzapfel, P. Novák and P. G. Bruce, *Journal of the American Chemical Society*, 2006, 128, 1390-1393.
4. R. Cao, J.-S. Lee, M. Liu and J. Cho, *Advanced Energy Materials*, 2012, **2**, 816-829.
5. V. Neburchilov, H. Wang, J. J. Martin and W. Qu, *Journal of Power Sources*, 2010, **195**, 1271-1291.
6. X. Wang, P. J. Sebastian, M. A. Smit, H. Yang and S. A. Gamboa, *Journal of Power Sources*, 2003, **124**, 278-284.
7. S. Velraj and J. H. Zhu, *Journal of Power Sources*, 2013, **227**, 48-52.
8. A. Inoishi, S. Ida, S. Uratani, T. Okano and T. Ishihara, *Physical Chemistry Chemical Physics*, 2012, **14**, 12818-12822.
9. I. C. Jang, Y. Hidaka and T. Ishihara, *Journal of Power Sources*, 2013, **244**, 606-609.
10. G. Du, X. Liu, Y. Zong, T. S. A. Hor, A. Yu and Z. Liu, *Nanoscale*, 2013, **5**, 4657-4661.
11. F. W. T. Goh, Z. Liu, X. Ge, Y. Zong, G. Du and T. S. A. Hor, *Electrochimica Acta*, 2013, **114**, 598-604.
12. S. Zhu, Z. Chen, B. Li, D. Higgins, H. Wang, H. Li and Z. Chen, *Electrochimica Acta*, 2011, **56**, 5080-5084.
13. J. Suntivich, K. J. May, H. A. Gasteiger, J. B. Goodenough and Y. Shao-Horn, *Science*, 2011, **334**, 1383-1385.
14. Z. Chen, A. Yu, D. Higgins, H. Li, H. Wang and Z. Chen, *Nano Letters*, 2012, **12**, 1946-1952.
15. F. Cheng and J. Chen, *Chemical Society Reviews*, 2012, **41**, 2172-2192.
16. K. Rida, M. A. Pena, E. Sastre and A. Martinez-Arias, *Journal of Rare Earths*, 2012, **30**, 210-216.
17. X. Wang and Y. D. Li, *Journal of the American Chemical Society*, 2002, **124**, 2880-2881.
18. X.-Y. Xue, L.-L. Xing, Y.-G. Wang and T.-H. Wang, *Solid State Sciences*, 2009, **11**, 2106-2110.
19. Y. Li, M. Gong, Y. Liang, J. Feng, J.-E. Kim, H. Wang, G. Hong, B. Zhang and H. Dai, *Nature* Communications, 2013, **4**, 7.
20. Y. Liang, H. Wang, J. Zhou, Y. Li, J. Wang, T. Regier and H. Dai, *Journal of the American Chemical Society*, 2012, 134, 3517-3523.
21. M. Khettab, S. Omeiri, D. Sellam, M. A. Ladjouzi and M. Trari, *Materials Chemistry and Physics*, 2012, **132**, 625-630.
22. Y. Cao, Z. Wei, J. He, J. Zang, Q. Zhang, M. Zheng and Q. Dong, *Energy & Environmental Science*, 2012, **5**, 9765-9768.

23. J. D. G. Fernandes, D. M. A. Melo, L. B. Zinner, C. M. Salustiano, Z. R. Silva, A. E. Martinelli, M. Cerqueira, C. A. Junior, E. Longo and M. I. B. Bernardi, *Materials Letters*, 2002, **53**, 122-125.
24. H. Xu, C. Wang, Y. Song, J. Zhu, Y. Xu, J. Yan, Y. Song and H. Li, *Chemical Engineering Journal*, 2014, **241**, 35-42.
25. K. Rida, A. Benabbas, F. Bouremmad, M. A. Pena and A. Martinez-Arias, *Catalysis* Communications, 2006, **7**, 963-968.
26. Z. Chen, A. Yu, R. Ahmed, H. Wang, H. Li and Z. Chen, *Electrochimica Acta*, 2012, **69**, 295-300.
27. X. Wu and K. Scott, *Journal of Power Sources*, 2012, **206**, 14-19.
28. F. Cheng, Y. Su, J. Liang, Z. Tao and J. Chen, *Chemistry of Materials*, 2010, **22**, 898-905.
29. X. Wu and K. Scott, *Journal of Materials Chemistry*, 2011, **21**, 12344-12351.
30. Y. Li and H. Dai, *Chemical Society Reviews*, 2014, **43**, 5257-5275.
31. G. Toussaint, P. Stevens, L. Akrour, R. Rouget and F. Fourgeot, *Metal/Air and Metal/Water Batteries*, 2010, **28**, 25-34.
32. J. Noack, C. Cremers, D. Bayer, J. Tuebke and K. Pinkwart, *Journal of Power Sources*, 2014, **253**, 397-403.

Figure captions:

Fig. 1 Schematic structure of the zinc-air battery system

Fig. 2 XRD pattern of (a) α-MnO_2; (b) $LaNiO_3$; (c) FTIR spectrum obtained for $LaNiO_3$; XPS spectra of α-MnO_2-$LaNiO_3$/CNTs hybrid: (d) survey spectrum; (e) C 1s; (f) O 1s; (g) La $3d_{5/2}$ and Ni $2p_{3/2}$; (h) Mn 2p

Fig. 3 Images of bifunctional catalyst for zinc/air battery, including SEM images of (a) α-MnO_2 nanorods; (b) $LaNiO_3$ nanoparticles; (c) bifunctional catalyst α-MnO_2-$LaNiO_3$/CNTs; and TEM images of (d) CNTs; (e) $LaNiO_3$/CNTs; (f) α-MnO_2/CNTs; (g) α-MnO_2-$LaNiO_3$/CNTs.

Fig. 4 ORR polarization curves of (a) $(\alpha\text{-}MnO_2)_x\text{-}(LaNiO_3)_y/CNT_{50\%}$ catalysts (x and y represent molar ratio, the weight ratio of CNT: 50%), and (b) $[(\alpha\text{-}MnO_2)_2\text{-}(LaNiO_3)_3]_w/(CNT)_z$ (w and z represent weight ratio). Scan rate: 10 mV s^{-1}, 1600 rpm; Solution: O_2-saturated 1.0 M KOH.

Fig. 5 (a) ORR polarization curves of $[(\alpha\text{-}MnO_2)_2\text{-}(LaNiO_3)_3]_{40\%}/(CNT)_{60\%}$ measured at different rotation rates in O_2-saturated 1.0 M KOH solution. (b) K-L plots measured at −0.40 V and −0.50 V *vs*. Hg/HgO.

Fig. 6 OER polarization curves of bifunctional catalysts (a) $(\alpha\text{-}MnO_2)_x\text{-}(LaNiO_3)_y/CNT$ (x and y represent molar ratio), and (b) $[(\alpha\text{-}MnO_2)_2\text{-}(LaNiO_3)_3]_w/(CNT)_z$ (w and z represent weight ratio). Scan rate: 10 mV s^{-1}; Solution: 1.0 M KOH.

Fig. 7 The ORR and OER activities of different ranges of (a) x:y and (b) w:z values of the catalyst $[(\alpha\text{-}MnO_2)_x\text{-}(LaNiO_3)_y]_w/(CNT)_z$.

Fig. 8 Repetitive cyclic voltammograms (1st, 30th, and 100th cycles) of the bifunctional catalyst $[(\alpha\text{-}MnO_2)_2\text{-}(LaNiO_3)_3]_{40\%}/(CNT)_{60\%}$. Scan rate: 10 mV s^{-1}; Solution: 1.0 M KOH.

Fig. 9 Polarization and power density curves of the zinc-air battery employed the bifunctional catalyst $[(\alpha\text{-}MnO_2)_2\text{-}(LaNiO_3)_3]_{40\%}/(CNT)_{60\%}$ (cell #1) and the catalyst sample $[(\alpha\text{-}MnO_2)_2\text{-}(LaNiO_3)_3]_{20\%}/(CNT)_{80\%}$ (cell #2).

Fig. 10 75 C-D cycles of the rechargeable zinc-air battery.

Fig. 11 (a) Comparison of Nyquist plots for zinc-air batteries at the initial, 50th and 75th C-D cycles. (b) Nyquist plots of zinc-air battery at different current loads. (c) Equivalent circuit model.

Figures

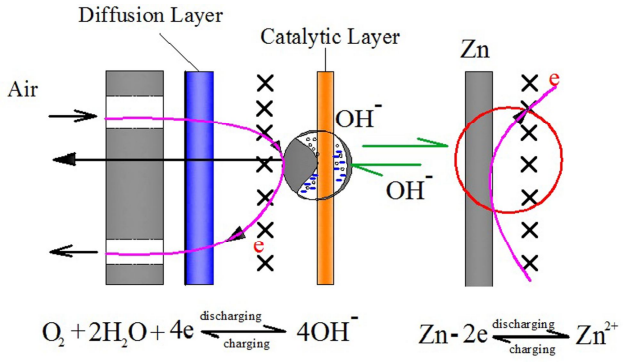

Fig. 1

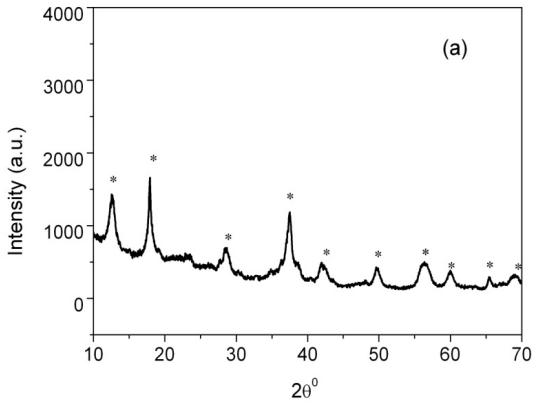

Fig. 2 (a)

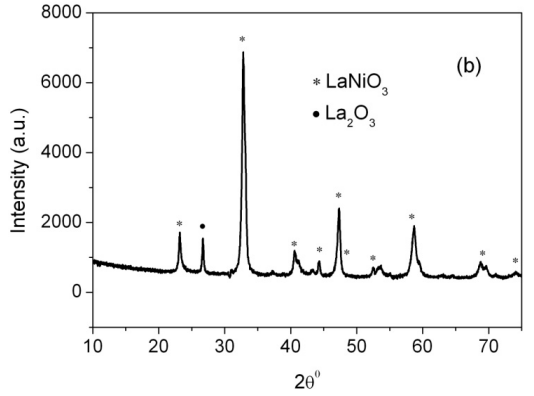

Fig. 2 (b)

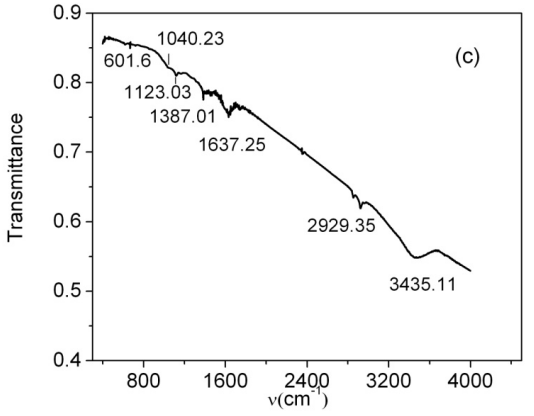

Fig. 2 (c)

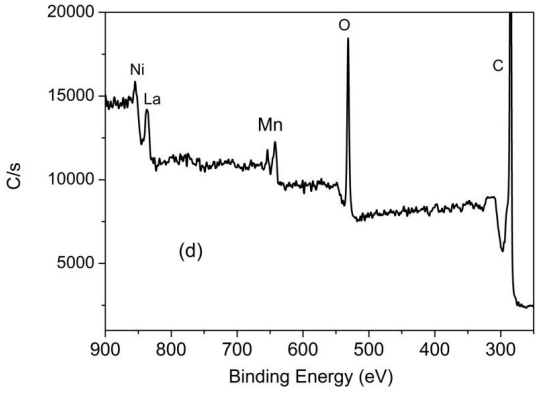

Fig. 2 (d)

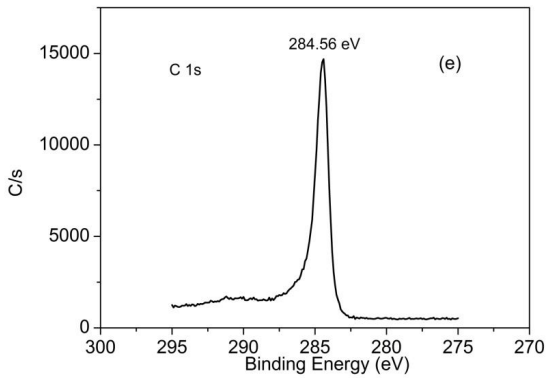

Fig. 2 (e)

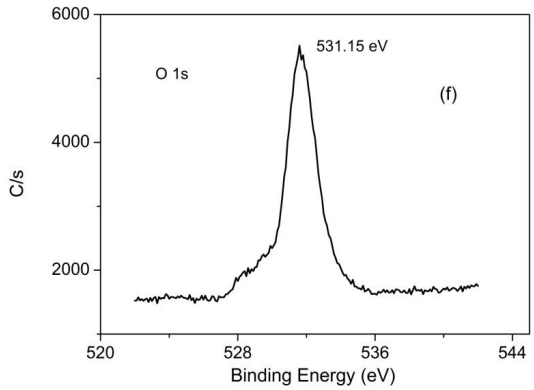

Fig. 2 (f)

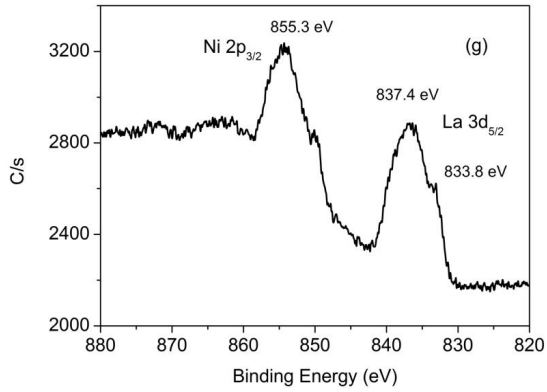

Fig. 2 (g)

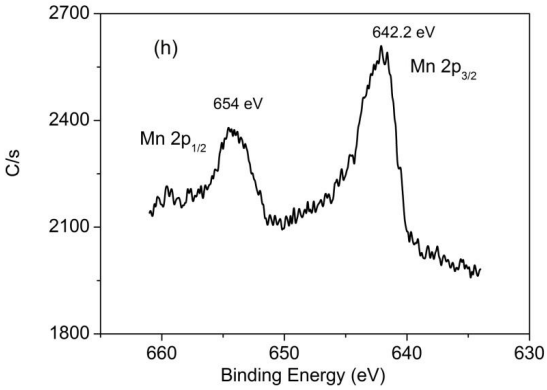

Fig. 2 (h)

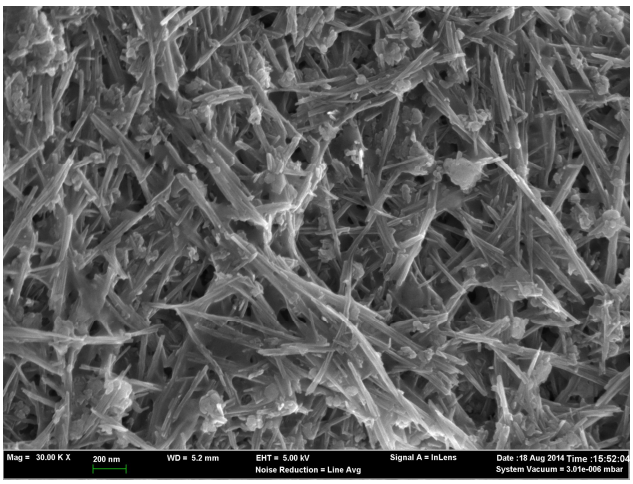

Fig. 3 (a)

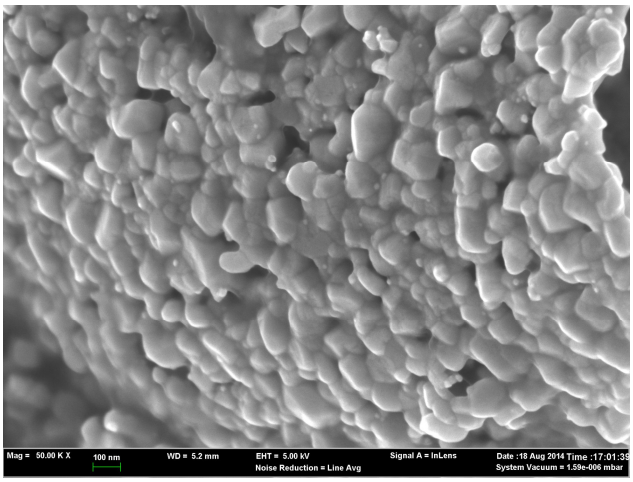

Fig. 3 (b)

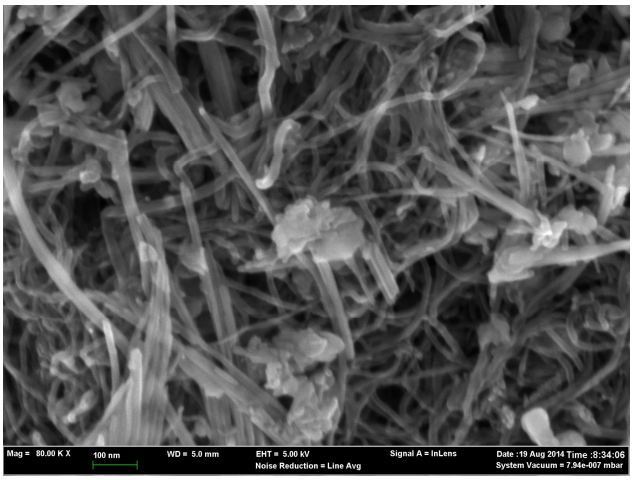

Fig. 3 (c)

Fig. 3 (d)

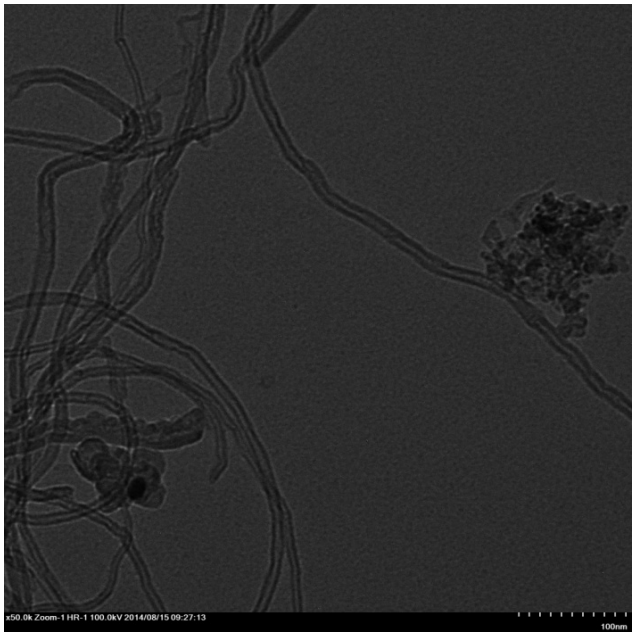

Fig. 3 (e)

Fig. 3 (f)

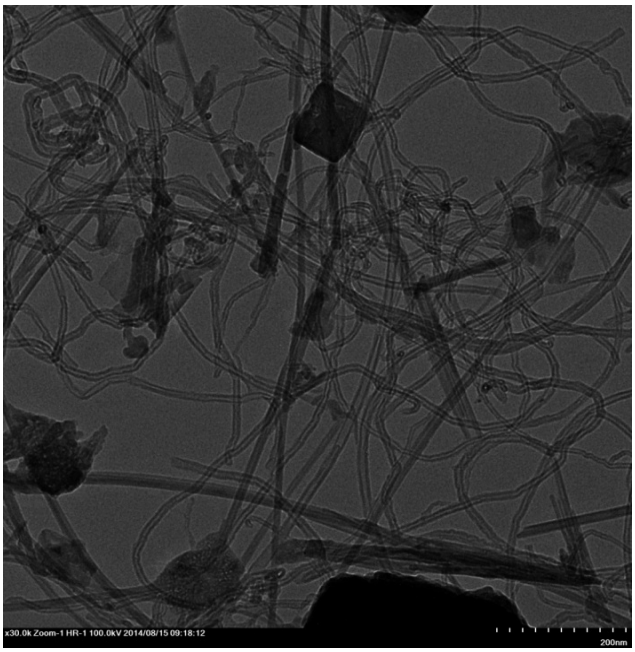

Fig. 3 (g)

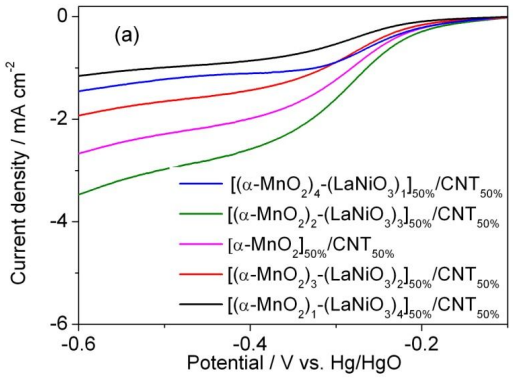

Fig. 4 (a)

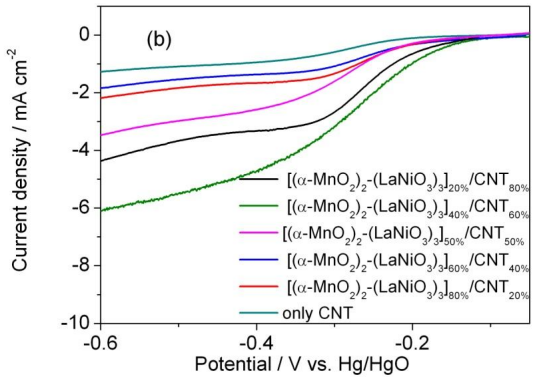

Fig. 4 (b)

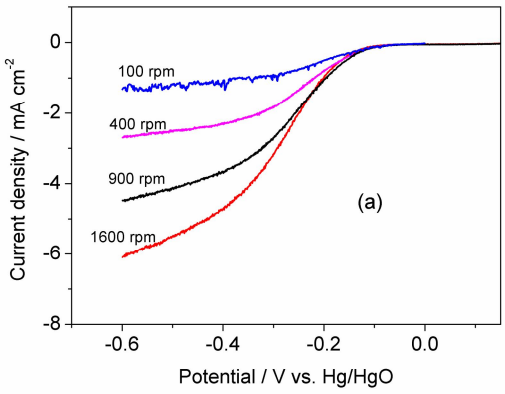

Fig. 5 (a)

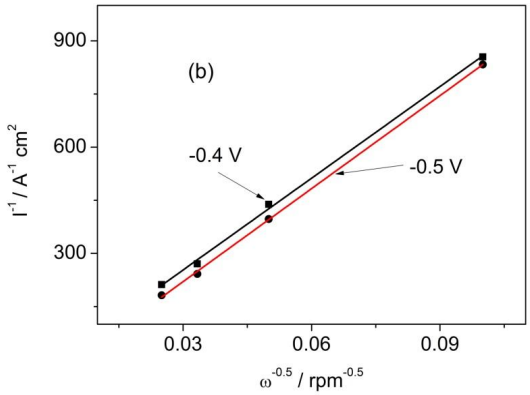

Fig. 5 (b)

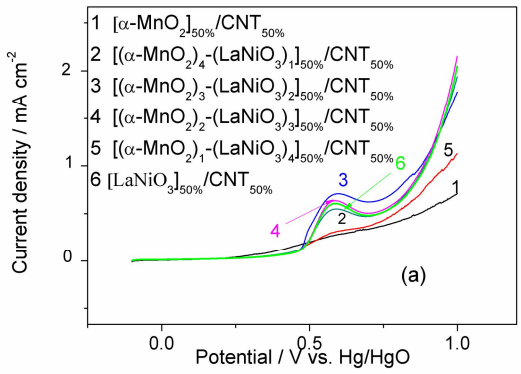

Fig. 6 (a)

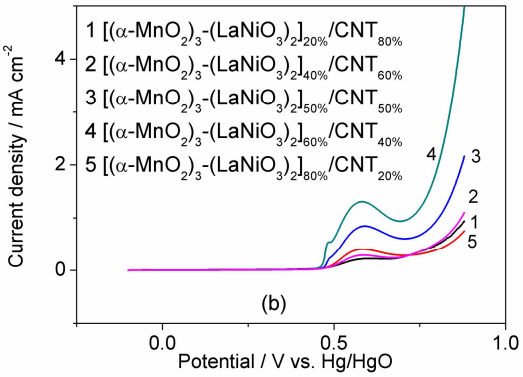

Fig. 6 (b)

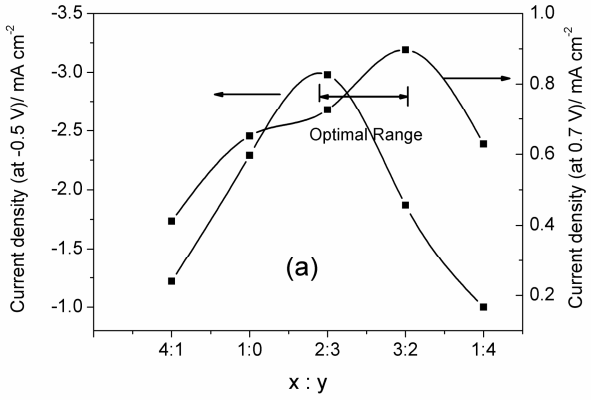

Fig. 7 (a)

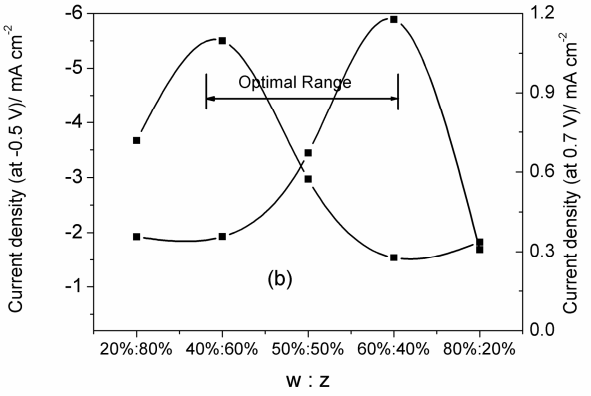

Fig. 7 (b)

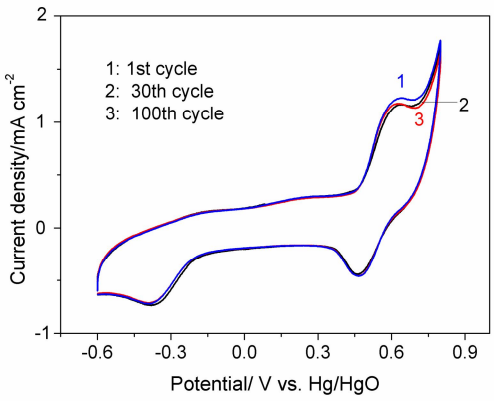

Fig. 8

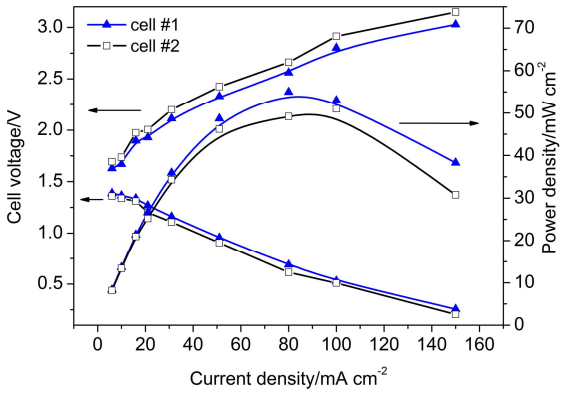

Fig. 9

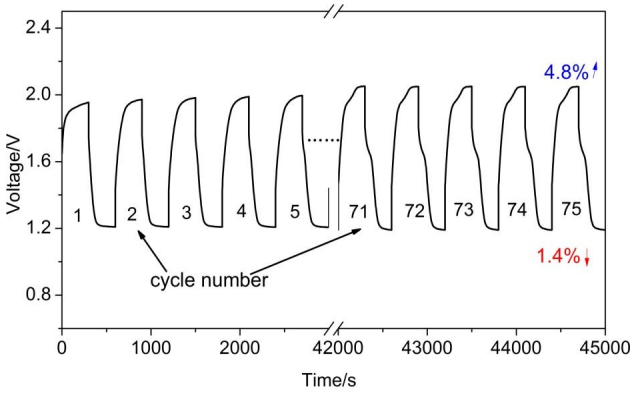

Fig. 10

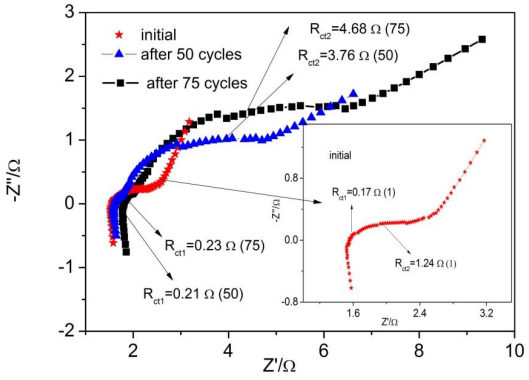

Fig. 11 (a)

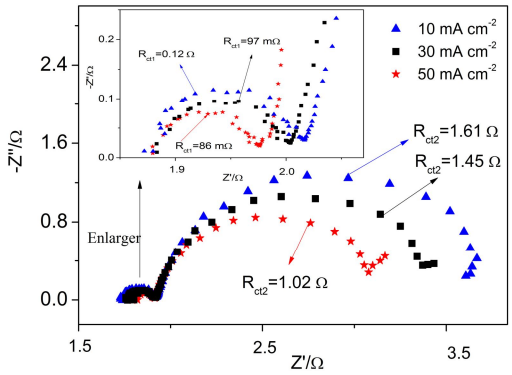

Fig. 11 (b)

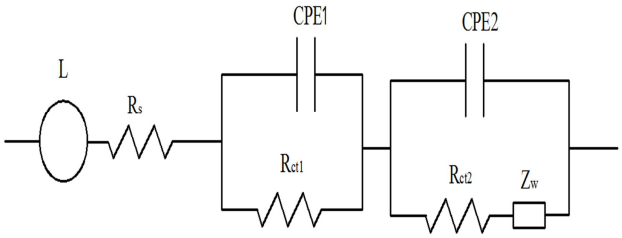

Fig. 11 (c)

Table

Table 1. Initial and final values of E_{charge} and $E_{discharge}$ of the zinc-air battery.

	Zinc-air battery		
	Initial value/V	Final value/V	Ratio of degradation
E_{charge}	1.954	2.048	4.8%
$E_{discharge}$	1.208	1.191	1.4%